Vol. 47 (2016) *ACTA PHYSICA POLONICA B* No 10

SPATIAL VARIATION OF WAVE PERIODS OF MAGNETOACOUSTIC-GRAVITY WAVES IN THE FLUX-TUBE

P. Chmielewski[a,b], K. Murawski[b], R. Sych[c]

[a]Institute of Plasma Physics and Laser Microfusion
Hery 23, 01-173 Warszawa, Poland
[b]Group of Astrophysics, UMCS
Radziszewskiego 10, 20-031 Lublin, Poland
[c]Institute of Solar-Terrestrial Physics
Siberian Branch of Russian Academy of Sciences
Irkutsk 664033, Russia

(Received April 7, 2016; revised version received July 29, 2016)

We study impulsively generated magnetoacoustic-gravity waves in the solar atmosphere permitted by diverged with height magnetic field lines which mimic magnetic field configuration of a flux-tube. We aim to find wave periods of magnetoacoustic-gravity waves along vertical and horizontal directions of the magnetic structure. Magnetohydrodynamic equations are solved numerically, there is used the Fourier analysis of temporal wave profiles, and there are performed some parametric studies of wave periods of magnetoacoustic-gravity waves as well as our numerical data are compared with the recent observational findings. The results of our parametric studies show that wave periods vary along vertical and horizontal directions. The numerical findings are in an agreement with the recent observational data for the wave-periods dependence along vertical and horizontal directions in the sunspot, made for the wavelength $\lambda = 1700$ Å. Our results form a basis for a construction of the seismological model, which determines the wave periods and their spatial variation in the sunspot.

DOI:10.5506/APhysPolB.47.2273

1. Introduction

In spite of a number of efforts, a scenario of magnetoacoustic-gravity waves propagation from the photosphere to the solar corona is still not sufficiently well-known; observations of sunspot oscillations raise lots of questions about spatial distribution of their wave periods. For instance, Yuan *et al.* [1] and Reznikova *et al.* [2] observed spatial dependence of the wave periods in sunspots and studied their variation along distance from the centre of the sunspot. In a gravitationally stratified atmosphere, the dispersion relation for magnetoacoustic waves, that can penetrate higher layers of the solar atmosphere, results in cut-off wave periods [3] that maps on their observability; thereby, we are not able to observe sufficiently long wave-period oscillations, which are filtered by the cut-off wave periods in structures like sunspots.

From studies of Fontenla *et al.* [4] and Jefferies *et al.* [5] we know that cut-off wave period of magnetoacoustic-gravity waves is increased by inclined magnetic field, which allows low-frequency waves to penetrate into the upper atmosphere. These findings were confirmed by Yuan *et al.* [1] in their studies of cut-off frequency of magnetoacoustic-gravity waves in the region of sunspot's umbra. They noticed that cut-off frequency is lowered by increased magnetic field inclination towards horizontal direction. However, three-minute oscillations observed in the chromosphere above sunspot by Botha *et al.* [6] were explained as a slow wave resonance in cavity between the photosphere and the transition region. They used one-dimensional (1D) model of the solar atmosphere with vertical magnetic field and found a relation between different umbral temperature profiles and frequency shift in sunspot oscillations over the solar cycle. Till now, there were performed many studies of MHD waves, which are directly connected with observed oscillatory motions in a sunspot and their neighbourhood. Periodic plasma motions in the sunspot umbra were investigated in a theoretical 2D model of the semi-infinite poly-tropic atmosphere permeated by the vertical magnetic field presented by Cally and Bogdan [7]. A propagation of magnetoacoustic waves in the photosphere and low chromosphere, lunched by a pulse in vertical and horizontal velocity components at the photospheric level in the model of small-size magnetic sunspot was a subject of investigations by Khomenko and Collados [8] and Felipe *et al.* [9]. They found that fast magnetohydrodynamic (MHD) wave mode is easily reflected at the transition region back to the photosphere, while slow mode propagates upwardly along lines of sunspot's magnetic field structure. Thus, the energy of hotter photospheric plasma can be transported to the upper atmosphere by slow mode MHD waves. On the other hand, the problem of properties of MHD waves travelling under the surface of sunspot's magnetic structure was investigated numerically by Khomenko *et al.* [10]. This studies allowed them to provide maps of the local Alfvén speed and local sound speed of the region below sunspot that are important to fully understand MHD wave behaviour and importance in and around a sunspot.

It should be noted that the existence of relationships between waves propagation in sunspot with initiation of flare energy release in the surrounding areas was recently obtained in [11, 12]. These processes are related to the initialization of periodic reconnections by slow magnetoacoustic waves [13] that propagate along magnetic waveguides (coronal magnetic structures) connecting sunspots with the flare regions. We observe that the wave motion in curved magnetic field lines leads to transverse oscillations [14] and energy release during reconnection near the local magnetic null points [15]. We can suppose that waves occurring around a sunspot can be triggers of solar flares. The knowledge of the fine spatial and frequency structure of oscillating sources allows us to understand the physical mechanisms of the running processes and make some conclusion about possibility of practical application as a short-term forecasting of solar flares.

Unfortunately, research mentioned above does not provide consistent and complete knowledge about reasons of the spatial variation of wave periods of magnetoacoustic-gravity waves in the sunspot-like structures. Nowadays, there arise questions about origins and way of formation of a distribution of the plasma oscillations in the region of sunspot.

Thus, the goal of this paper is to numerically simulate magnetoacoustic-gravity waves in the solar atmosphere and to examine spatial dependence of their wave periods along horizontal and vertical directions of the diverged magnetic field configuration which mimics a magnetic field of a sunspot. We present a general structure of wave profiles, emphasizing a dependence of a wave period on a spatial location of a detected signal, and compare our numerical findings to recent observational data of sunspots, which reveal that a wave period of magnetoacoustic waves grows with the radial distance from the centre of the sunspot [1, 2].

Our paper is organized as follows. A numerical model of the solar atmosphere is described in Sec. 2. In the following section, we present our numerical results for diverged magnetic field. Finally, we compare our results to the observational data in Sec. 4 and complete our paper by conclusions in Sec. 5.

2. Numerical model of the solar atmosphere

2.1. MHD equations

Our model of the solar atmosphere contains a gravitationally-stratified magneto-plasma, which is described by the following set of ideal magnetohydrodynamic (MHD) equations:

$$\frac{\partial \varrho}{\partial t} + \nabla \cdot (\varrho \boldsymbol{V}) = 0\,, \tag{1}$$

$$\varrho \frac{\partial \boldsymbol{V}}{\partial t} + \varrho\,(\boldsymbol{V} \cdot \nabla)\,\boldsymbol{V} = -\nabla p + \frac{1}{\mu}(\nabla \times \boldsymbol{B}) \times \boldsymbol{B} + \varrho \boldsymbol{g}\,, \tag{2}$$

$$\frac{\partial \boldsymbol{B}}{\partial t} = \nabla \times (\boldsymbol{V} \times \boldsymbol{B})\,, \tag{3}$$

$$\nabla \cdot \boldsymbol{B} = 0\,, \tag{4}$$

$$\frac{\partial p}{\partial t} + \boldsymbol{V} \cdot \nabla p = -\gamma p \nabla \cdot \boldsymbol{V}\,, \tag{5}$$

$$p = \frac{k_{\rm B}}{m} \varrho T\,. \tag{6}$$

Here, ϱ is the mass density, $\boldsymbol{V}$ and $\boldsymbol{B}$ are vectors of respectively the flow velocity and the magnetic field, p is a gas pressure, μ is the magnetic permeability of the plasma, $\gamma = 5/3$ is the adiabatic index, $\boldsymbol{g} = (0, -g, 0)$ is a vector of gravitational acceleration with its value $g = 274$ m s^{-2}, T is a temperature, m is a mean particle mass that is specified by a mean molecular weight equal to 1.24, and $k_{\rm B}$ is a Boltzmann's constant. Here, we considered the simplest conceivable model of solar plasma which consists of MHD equations. More realistic models such as multi-fluid and/or kinetic can be used for much shorter spatial regions and temporal scales. They also require much more powerful computers and a development of numerical methods to be solved.

Notice that in our equations there is no cooling term, which results from the effect of radiative cooling. However, the cooling term plays an important role in the lower layers of the solar atmosphere and at the transition region, it has no qualitative influence on the MHD waves behaviour. Note that a cooling term would lead to large flow and, as a result, to evolution of the system in time. Thus, the waves signal would be deeply hidden in the signal resulted from the evolution of the system in time. A model containing a linear wave equation with a radiative cooling term for adequate fitting the observed phase delay and wave amplitude variation with height in both sunspots and pores was constructed by Centeno *et al.* [16, 17].

2.2. Initial conditions

2.2.1. A model of the solar atmosphere

In our two-dimensional (2D) model, we assume that the solar atmosphere is in the static equilibrium ($\boldsymbol{V}_{\rm e} = \boldsymbol{0}$) with force- and current-free magnetic field, *i.e.*,

$$(\nabla \times \boldsymbol{B}_{\rm e}) \times \boldsymbol{B}_{\rm e} = \boldsymbol{0}\,, \qquad \nabla \times \boldsymbol{B}_{\rm e} = \boldsymbol{0}\,, \tag{7}$$

where $\boldsymbol{B}_{\rm e}$ is the equilibrium magnetic field. We consider the model of diverged magnetic field developed by Low [18],

$$\boldsymbol{B}_{\rm e}(x, y) = \nabla \times (A\hat{\boldsymbol{z}})\,, \tag{8}$$

which is defined by the magnetic flux function

$$A(x, y) = \frac{x(y_{\rm ref} - b)^2}{(y - b)^2 + x^2} B_{\rm ref}\,. \tag{9}$$

Here, $\hat{\boldsymbol{z}}$ is a unit vector along the z-direction and $B_{\rm ref}$ is the magnetic field at the reference level, $y_{\rm ref} = 10$ Mm. The magnetic field, whose vectors are displayed in Fig. 1, is defined by the magnetic pole that is located at the point $(0, b)$, where b we set and hold fixed to -10 Mm. The diverged magnetic field line configuration mimics curved magnetic field of the sunspot. Note that at a given altitude y, magnetic field is strongest and essentially vertical around the line $x = 0$ Mm. Further out the magnetic field declines with larger values of $|x|$, revealing its curved structure.

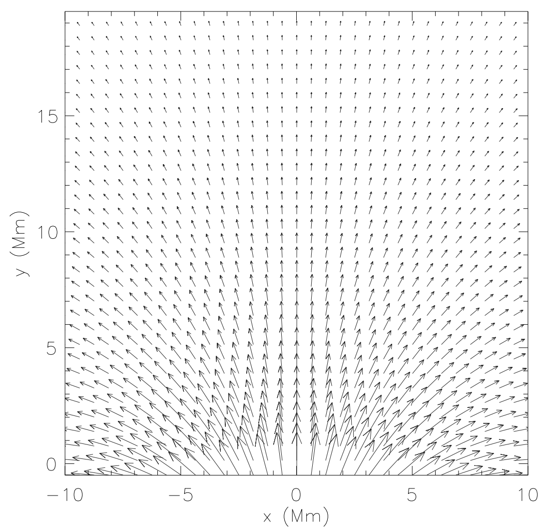

Fig. 1. Vectors of the magnetic field.

As a result of Eq. (7), the pressure gradient is balanced by the gravity force

$$-\nabla p_{\rm e} + \varrho_{\rm e}\boldsymbol{g} = \boldsymbol{0}\,. \tag{10}$$

Using the ideal-gas law of Eq. (6) and the y-component of the hydrostatic pressure balance indicated by Eq. (10), we express equilibrium gas pressure and mass density as

$$p_{\rm e}(y) = p_0 \,\exp\left(-\int\limits_{y_{\rm ref}}^{y} \frac{{\rm d}y'}{\Lambda(y')}\right)\,, \qquad \varrho_{\rm e}(y) = \frac{p_{\rm e}(y)}{g\Lambda(y)}\,. \tag{11}$$

Here,

$$\Lambda(y) = \frac{k_{\rm B}T_{\rm e}(y)}{mg} \tag{12}$$

is the pressure scale-height, and p_0 denotes the gas pressure at the reference level.

We adopt a realistic, semi-empirical model of the plasma temperature developed by Avrett and Loeser [19], which is displayed in Fig. 2, the top-left panel. Temperature declines with y until $y \approx 0.6$ Mm, where T reaches its minimum, $T \approx 4300$ K. Higher up, the temperature raises up with y and at the transition region, that is located at $y \simeq 2.1$ Mm, experiences sudden growth to about 2×10^6 K at $y = 10$ Mm in the solar corona. Profile of the temperature determines uniquely the equilibrium mass density and gas pressure profiles (Eq. (11)). Both $\varrho_\mathrm{e}(y)$ (Fig. 2, the top-right panel) and $p_\mathrm{e}(y)$ (not shown) fall off with y.

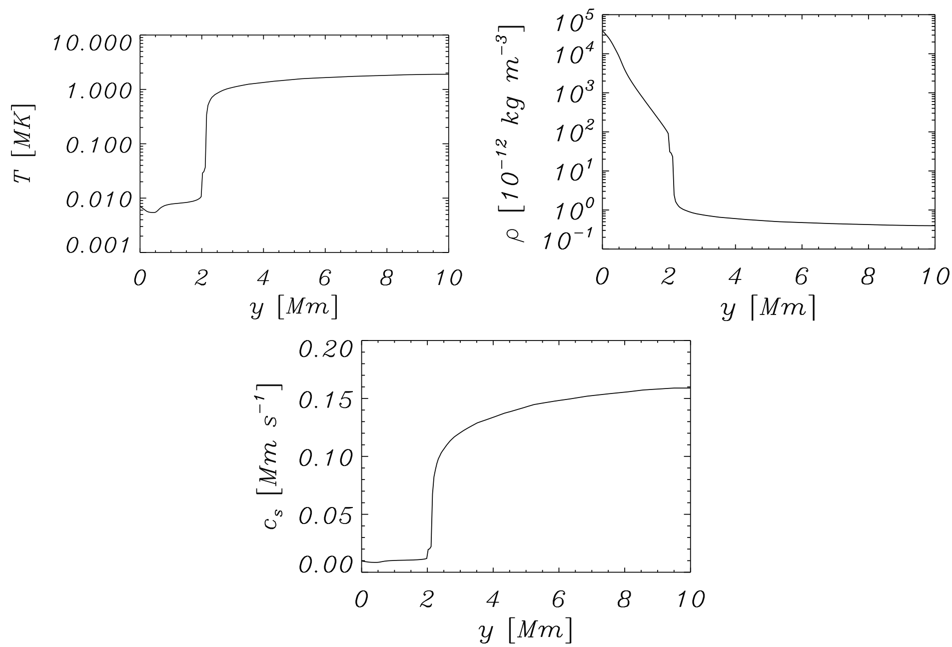

Fig. 2. Equilibrium profiles of the temperature (the top-left panel), the mass density (the top-right panel) and the sound speed (the bottom panel).

In this model, the sound speed, c_s, varies only with y and is expressed as follows:

$$c_\mathrm{s}(y) = \sqrt{\frac{\gamma p_\mathrm{e}(y)}{\rho_\mathrm{e}(y)}} \,. \tag{13}$$

The sound speed profile follows the temperature profile (Fig. 2, the bottom panel) and, as a result, reveals that sound wave propagating upwardly from the chromosphere to the solar corona experiences sudden acceleration at the transition region due to increase of the sound speed there.

In Fig. 3, we present spatial variation of logarithm of the plasma β, which is the ratio of plasma pressure and magnetic pressure

$$\beta(x, y) = \frac{p_{\mathrm{e}}(x, y)}{\frac{B_{\mathrm{e}}^2(x,y)}{2\mu}} \,. \tag{14}$$

The plasma β attains large values in the photosphere and chromosphere far from $x = 0$ Mm and low β above the transition region for small values of $|x|$. In the solar corona, β grows up with $|x|$ and y, which results from the faster fall off of the magnetic pressure than the gas pressure there. The value of plasma β plays an important part in the process of magnetoacoustic-gravity wave propagation, channelling the wave-fronts along the magnetic field lines under low values of β, what we describe in Sec. 3.

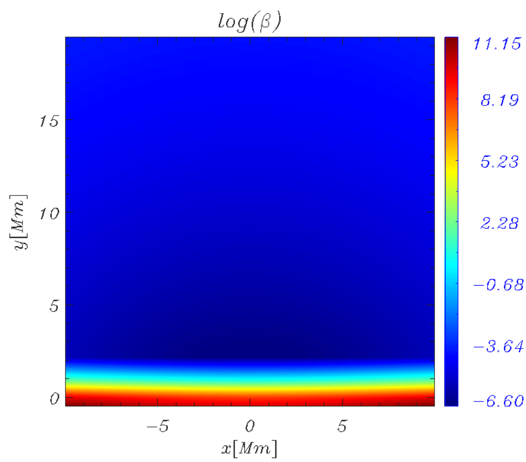

Fig. 3. Spatial profile of $\log(\beta(x, y))$.

2.2.2. Initial perturbations

The model equilibrium described above is perturbed initially at $t = 0$ s by a Gaussian pulse in the y-component of the velocity given by

$$V_y(x, y, t = 0) = A_v \exp\left[-\frac{x^2 + (y - y_0)^2}{w^2}\right] , \tag{15}$$

where A_v is the amplitude of the pulse, $(0, y_0)$ is its initial position and w denotes its width. We set and hold fixed $w = 0.5$ Mm, and $y_0 = 0.5$ Mm, while A_v is allowed to attain its value either 0.5 km s^{-1} or 2 km s^{-1}. Notice that $V_x(x, y, t = 0) = V_z(x, y, t = 0) = 0$. A location and a shape of the initial pulse is illustrated in Fig. 4 as a black (red-brown) patch.

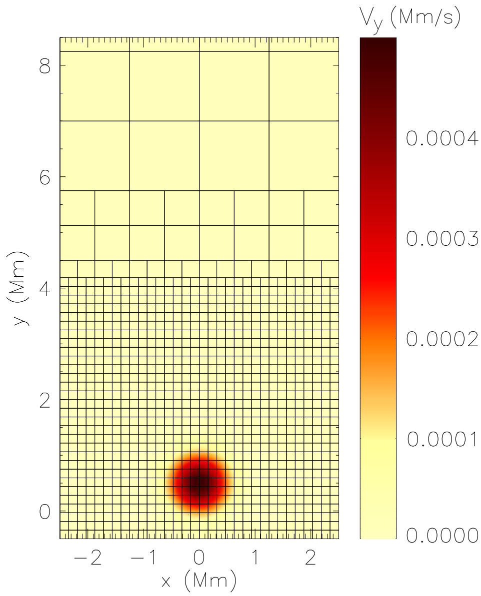

Fig. 4. (Colour on-line) The initial pulse (black/colour patch) and numerical blocks (solid lines) at $t = 0$ s.

3. Numerical results

To solve numerically equations (1)–(6), we use the FLASH code [20–23], which applies a third-order unsplit Godunov solver with various slope limiters and Riemann solvers as well as Adaptive Mesh Refinement (AMR) [24]. Controlling the numerical errors in mass density is a base of the mesh refinement strategy. We use the minmod slope limiter and approximate Harten–Lax–van Leer-Discontinuities (HLLD) Riemann solver [23]. The simulation box is set as $(-10\ \mathrm{Mm}, 10\ \mathrm{Mm}) \times (-0.5\ \mathrm{Mm}, 59.5\ \mathrm{Mm})$ and boundary conditions are imposed fixed in time for all plasma quantities in the x- and y-directions. The AMR grid with a minimum (maximum) level of refinement set to 3 (6) was used in the presented studies. We performed the grid convergence studies by refining the grid; as the results remained essentially invariant, we used the present grid for the presentation of numerical results. Every numerical block consists of 8×8 identical numerical cells. Blocks are finest below the level of $y = 4$ Mm (Fig. 4). The best spatial resolution is $\Delta x = \Delta y = 15.625$ km, which results in an excellent resolution of vital spatial profiles and greatly reduces the numerical diffusion at these locations.

As a result of the perturbation of the chromosphere by the initial pulse in V_y (Eq. 15), there arise magnetoacoustic-gravity waves (Fig. 5). Along $x = 0$ Mm (Fig. 1), there is an almost vertical magnetic field which in a low plasma β region (for $y > 1.12$ Mm) channels the slow magnetoacoustic waves in the vertical direction, resulting in the intensification of the wave propagation in the y-direction. The shape of the initial pulse gradually changes into the bagel shape (Fig. 5, top-left). Here, vectors of velocity (V_x, V_y) show plasma flow resulting from magnetoacustic-gravity waves. While the wave passes the transition region, it experiences rapid acceleration (Fig. 5, top-middle) that is caused by the increase in the sound speed there (Fig. 2, the bottom panel). It also suffers a sudden growth in amplitude up to $V_y(t = 180\ \mathrm{s}) \simeq 3\ \mathrm{km\ s^{-1}}$ at $y \simeq 3$ Mm (Fig. 5, top-middle). In the top-right panel of Fig. 5, we observe raising of the second pulse from the launching point (0 Mm, 0.5 Mm), following the first one that is a result of oscillating medium perturbed at $t = 0$ s by the initial pulse (*e.g.* [25]). Above the transition region, the amplitude of the pulse increases abruptly reaching $V_y(t = 420\ \mathrm{s}) \simeq 30\ \mathrm{km\ s^{-1}}$ at $y = 17$ Mm (bottom-left). Here, we observe plasma propagating downwards at $y = 2.5$ Mm, that hits the transition region. At $t = 480$ s (Fig. 5, bottom-middle), the next wave front entered already the solar corona, which we later observe at $y = 18$ Mm (bottom-right). The bottom-left panel shows formation of the third wave front at $y \sim 2$ Mm propagating to the solar corona (Fig. 5, bottom-right).

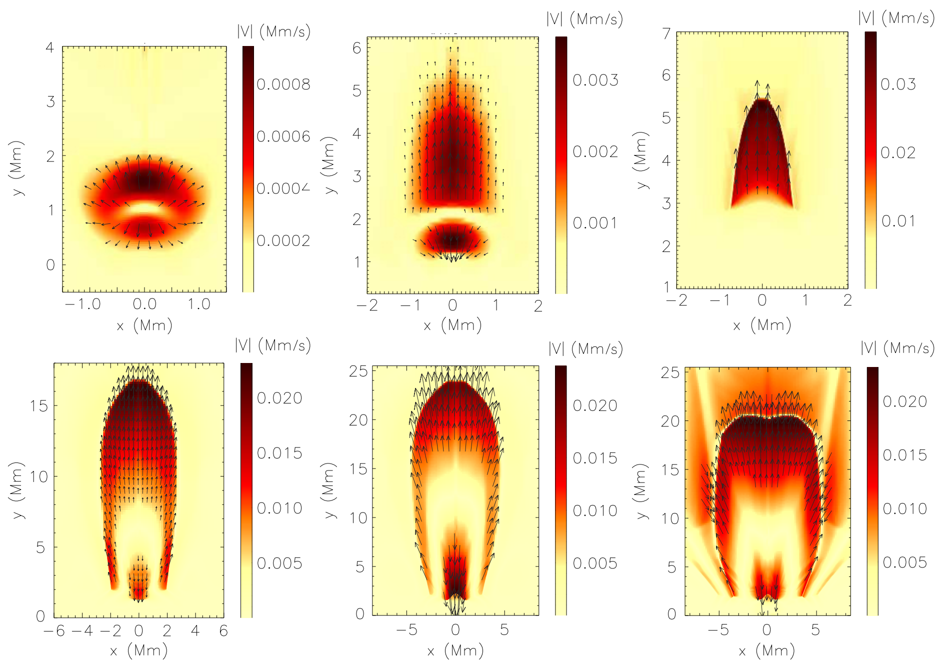

Fig. 5. Spatial profiles of total velocity $|\boldsymbol{V}|$ overlaid by velocity vectors at $t = 100$ s (top-left), $t = 180$ s (top-middle), $t = 300$ s (top-right), $t = 420$ s (bottom-left), $t = 480$ s (bottom-middle), and $t = 680$ s (bottom-right) for the case of $A_v = 0.5\ \mathrm{km\ s^{-1}}$.

Propagating wave fronts are well-observed at time signatures of y-component of the velocity. We analyse time signal of $V_y(x = 0, y, t)$ that is collected at two altitudes: $y = 2$ Mm and 3 Mm (Fig. 6). As an effect of the propagating magnetoacoustic-gravity wave, we observe oscillations of V_y. Note that vertical velocity variations are essentially stable for small initial pulse amplitude, $A_v = 0,5$ km s^{-1} (left panel), while they suffer attenuation with time in the case of large amplitude perturbation (right panel), what was reported by Suematsu *et al.* [26], Botha *et al.* [6] and Murawski *et al.* [27]. Additionally, as the equilibrium mass density decreases with altitude, V_y grows with height revealing shocks (*e.g.* [28]).

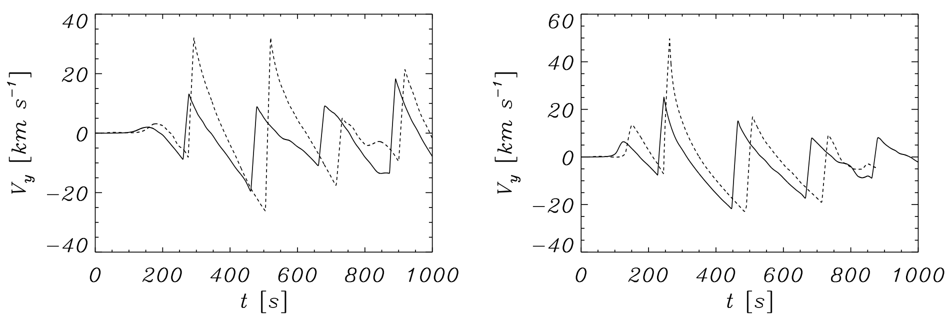

Fig. 6. Time-signatures of V_y collected at $y = 2$ Mm (the solid line) and $y = 3$ Mm (the dashed line) for $x = 0$ Mm, $A_v = 0.5$ km s^{-1} (left panel), and $A_v = 2$ km s^{-1} (right panel).

3.1. Wave-periods variation along the vertical direction

As a result of the Fourier analysis of the wave oscillations detected at the spatial points at which we collected signals in V_y (Fig. 6), we obtain power spectra (Fig. 7) that allow us to determine the dominant wave period P, for each detection point. In Fig. 8, we present a dependence of P on altitude y. Note that values of P are within the range of about 200 and 250 seconds, that corresponds to approximately 3- and 4-minutes oscillations. For low values of y, we observe a decrease of P down to $P \simeq 200$ s at $y \simeq 2$ Mm for $A_v = 0.5$ km s^{-1} (crossed circles) and at $y \simeq 1$ Mm for $A_v = 2$ km s^{-1} (crossed diamonds). Higher up, the wave periods of magnetoacustic-gravity waves generated by the large amplitude pulse ($A_v = 2$ km s^{-1}) grow to about 250 s at $y \simeq 7$ Mm (Fig. 8, diamonds). The wave periods gradually grow with height for $A_v = 2$ km s^{-1} and agree with the observational data of Yuan *et al.* [1] represented by the full squares in Fig. 8. On the other hand, P for small amplitude perturbation ($A_v = 0.5$ km s^{-1}) grows only till $P \simeq 216$ s and above the level of $y = 4.5$ Mm, it remains essentially constant.

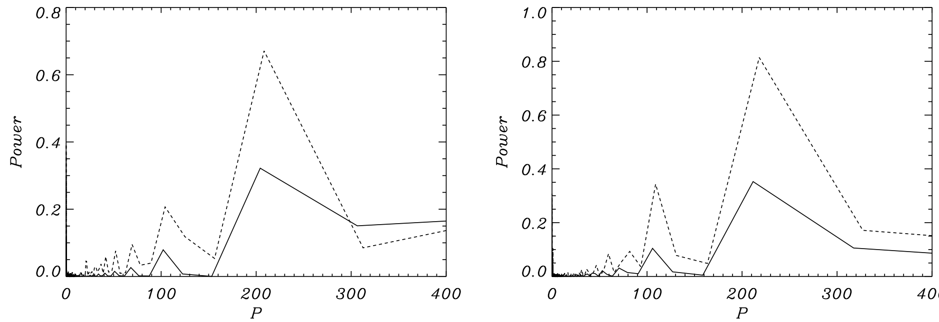

Fig. 7. The Fourier power spectra *vs.* wave periods for the wave signals collected at $y = 2$ Mm (the solid line) and $y = 3$ Mm (the dashed line) at $x = 0$ Mm for $A_v = 0.5$ km s^{-1}.

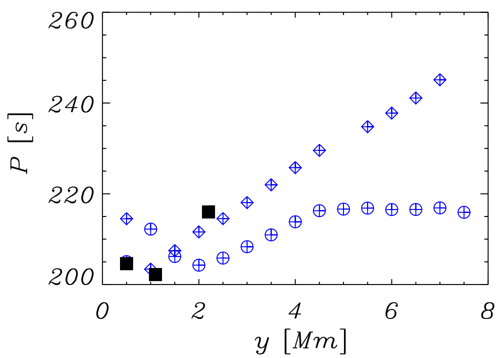

Fig. 8. The dominant wave periods for $A_v = 0.5$ km s^{-1} (crossed circles) and $A_v = 2$ km s^{-1} (crossed diamonds) at $x = 0$ Mm *vs.* y. Full squares represent cut-off wave periods obtained by Yuan *et al.* [1].

3.2. Wave-periods variation along the horizontal direction

A dependence of the wave periods on horizontal coordinate is illustrated in Fig. 9. The left panels correspond to dominant wave periods determined at levels $y = 2$ Mm, while the right panels for $y = 2.5$ Mm. The wave periods obtained in the numerical simulations (diamonds and circles) vary from about 160 s to 205 s for $A_v = 0.5$ km s^{-1} and from 170 s to 220 s for $A_v = 2$ km s^{-1}. Our results reveal a gradual decrease of dominant wave periods of magnetoacoustic-gravity waves with horizontal direction. It is noteworthy that pulses with large initial amplitude (Fig. 9, bottom panels, diamonds) modify the horizontal wave-periods dependence, resulting in increasing of P for small values of $|x|$, where P slightly grows up and exhibits a local maximum of $P \simeq 220$ s. For larger x, the wave periods fall off with x up to about $P = 160$ s independently on amplitude and altitude of the initial pulse.

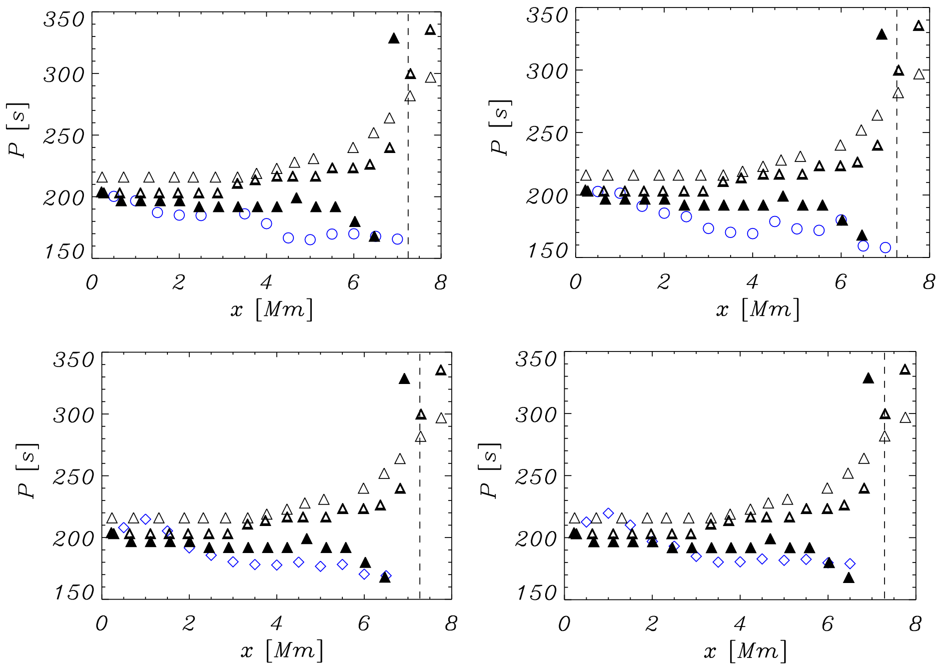

Fig. 9. The wave periods for $A_v = 0.5\,\mathrm{km\,s^{-1}}$ (top panels, circles) and $A_v = 2\,\mathrm{km\,s^{-1}}$ (bottom panels, diamonds) at $y = 2$ Mm (left panels) and $y = 2.5$ Mm (right panels) *vs.* horizontal coordinate x. Open triangles represent observational cut-off wave periods obtained for $\lambda = 304$ Å ($y \simeq 2.2$ Mm), open bold triangles for $\lambda = 1600$ Å ($y \simeq 1.1$ Mm) and full triangles for $\lambda = 1700$ Å ($y \simeq 0.5$ Mm). Dashed vertical line corresponds to the umbra–penumbra boundary.

Similarity of the magnetic field configuration chosen in the numerical model of the solar atmosphere to the structure of magnetic field lines in the sole axisymmetric sunspot induces us to compare our findings with cut-off wave periods obtained by Yuan *et al.* [1] in their analysis of observational data of wave periods near the sunspot for wavelength $\lambda = 304$ Å (Fig. 9, open triangles), that corresponds to $y \simeq 2.2$ Mm, for $\lambda = 1600$ Å (Fig. 9, open bold triangles), that corresponds to $y \simeq 1.1$ Mm and for $\lambda = 1700$ Å (Fig. 9, full triangles), that corresponds to $y \simeq 0.5$ Mm. We observe that both, the numerical and observational wave periods are in the range of 3–4 minutes for small values of $|x|$, while for $|x| > 6.5$ Mm the wave-periods values of observational data raise abruptly. However, we cannot ascertain the wave-periods growth above $|x| = 6.5$ Mm from the numerical simulations, due to a high level of numerical noise there.

3.3. Analytical findings of the wave-periods variation along the vertical direction

Using Eqs. (2) and (5), we can find the relation describing the cut-off wave periods along y-axis in the plasma of the solar atmosphere with large β called Klein–Gordon equation

$$\frac{\partial^2 Q}{\partial t^2} - c_{\rm s}^2(y)\frac{\partial^2 Q}{\partial y^2} = -\Omega^2(y)Q\,, \tag{16}$$

where

$$Q(y,t) = \sqrt{\frac{\varrho(y)c_{\rm s}^2(y)}{\varrho(y_{\rm ref})c_{\rm s}^2(y_{\rm ref})}}V_y(y,t)\,, \tag{17}$$

$$\Omega(y) = \frac{c_{\rm s}(y)}{2\Lambda(y)}\sqrt{1+2\frac{\partial\Lambda(y)}{\partial y}}\,, \qquad \Lambda(y) = \frac{c_{\rm s}^2}{\gamma g}\,. \tag{18}$$

Here, Ω is the frequency of waves in the form of $V_y \sim \exp i(ky \pm \omega t)$, where ω is the wave frequency, k is the wave vector and $i = \sqrt{-1}$. There can be derived an approximate dispersion relation for small varying $c_{\rm s}(y)$

$$\omega^2 = c_{\rm s}^2 k^2 + \Omega^2\,. \tag{19}$$

Having $c_{\rm s}^2 k^2 \geq 0$, we obtain a condition, $\omega \geq \Omega = \Omega_{\rm ac}$, that defines minimal frequency of propagating waves called acoustic cut-off frequency. Thus, we get a relation $P_{\rm ac} \geq P$, which limits wave periods of waves to propagate along y-axis with maximal acoustic cut-off wave periods, $P_{\rm ac} = 2\pi/\Omega_{\rm ac}$. Hence, the perturbed plasma in our model of the solar atmosphere at $y = 0.5$ Mm, where $\beta \gg 1$, by pulse in y-component of plasma velocity, generates wave fronts propagating upwardly to the solar corona with sound speed, $c_{\rm s}$. In the initial point, the perturbed plasma starts to oscillate with cut-off frequency generating next wave fronts observed in Fig. 5.

Applying to Eq. (18) the values of plasma parameters, such as the mass density and pressure obtained in the numerical simulation, we find variation with altitude of the acoustic cut-off wave periods, $P_{\rm ac} = 2\pi/\Omega_{\rm ac}$, which we present in Fig. 10. This analytical acoustic cut-off wave period (dashed line) provide the theoretical quantity that we can refer to. Notice that at the beginning, the values of acoustic cut-off wave periods (dashed line) decrease from $P_{\rm ac} \simeq 230$ s till $P_{\rm ac} \simeq 150$ s and then start to increase exponentially with y at $y \simeq 2$ Mm. Analysing variation of $P(y)$ (Fig. 10), we should remember about assumption of large β plasma ($\beta \gg 1$), for which we defined $\Omega_{\rm ac}$. Because of large β assumption, values of acoustic cut-off wave periods above $y(\beta = 1) = 1.124$ Mm show only expected changes of $P_{\rm ac}$ with altitude. For large plasma β ($|x| < 1.12$ Mm), the wave-periods values obtained in numerical simulations (Fig. 9) and the analytically calculated acoustic cut-off wave periods are close to 3–4 minutes. The results of numerical simulations agree with observational analysis of plasma oscillations [1] for $\lambda = 1700$ Å (Fig. 9, full triangles) that corresponds to $y = 0.5$ Mm, for which in our numerical model the plasma β is larger than one. For larger values of y, the plasma β decreases. Additionally, passing wave fronts, in particular shock waves, modify plasma property of the solar atmosphere, what affects magnetoacoustic-gravity wave propagation, as well as the wave periods.

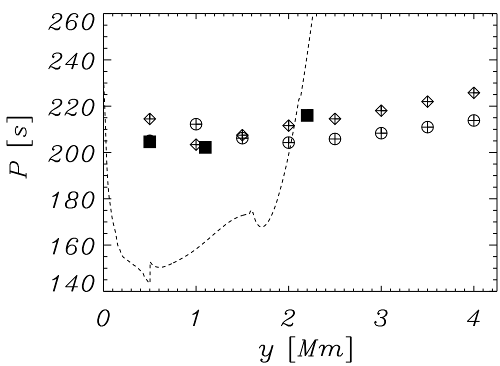

Fig. 10. The analytical cut-off wave periods *vs.* y for $b = -10$ Mm and $x = 0$ Mm. Dashed line corresponds to the acoustic cut-off wave periods, $P_{\rm ac}$.

3.4. Wave energy transport to the solar corona

We perform an analysis of the energy flux changes along vertical and horizontal directions. The energy flux is defined by the approximate formula derived by Vigeesh *et al.* [29] for a gravity-free medium

$$\boldsymbol{E}_{\rm flux}(x,y) \approx \left[\varrho c_t V_x^2, \varrho c_{\rm s} V_y^2\right] , \tag{20}$$

where $c_{\rm A}$ and $c_t = \sqrt{c_{\rm s}^2 + c_{\rm A}^2}$ are Alfvén and fast speed, respectively. Here, values of the mass density as well as x- and y-component of plasma velocity collected at different points are averaged over the time. The changes with height of the energy flux generated by propagating magnetoacoustic wave are presented in Fig. 11. We observe that the energy, which the wave is able to conveyed to the plasma, rises with height in the lower layers of the solar atmosphere. Above the transition region at $y = 2.5$ Mm, the energy flux reaches its maximum equal to 5.2×10^4 J m^{-3} s^{-1} for $A_v = 0.5$ km s^{-1} (Fig. 11, left panel) and 49.8×10^4 J m^{-3} s^{-1} for $A_v = 2$ km s^{-1} (Fig. 11, right panel). Thus, above the transition region, the plasma motion forced by the passing magnetoacoustic wave, decreases with altitude and we observe that $E_{\rm flux}$ drops asymptotically with height to zero reaching at $y =$

5 Mm the value 0.7×10^4 J m^{-3} s^{-1} for $A_v = 0.5$ km s^{-1} (left panel) and 9.2×10^4 J m^{-3} s^{-1} for $A_v = 2$ km s^{-1} (right panel). Notice that close below the transition region the energy flux suffers fall off of its value and next abruptly increases to its maximum.

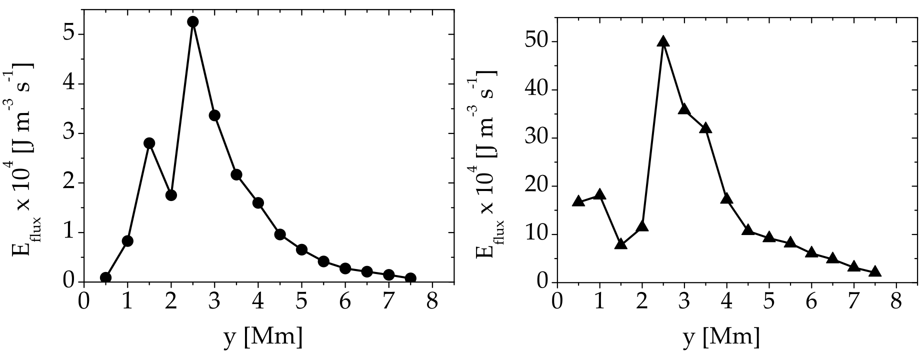

Fig. 11. Energy flux *vs.* height for $A_v = 0.5$ km s^{-1} (left panel) and $A_v = 2$ km s^{-1} (right panel) at $x = 0$ Mm.

However, the distribution of the energy flux values in the horizontal direction reveals a global depletion with the distance from $x = 0$ Mm, it has a maximum in $x = 1.5$ Mm, then it falls off abruptly to $E_{\rm flux} = 0.35 \times 10^4$ J m^{-3} s^{-1} at $x = 3$ Mm and next it slowly fades out (Fig. 12). Here, the attenuation of the energy flux is connected with significant decrease of the vertical component of plasma motion with x.

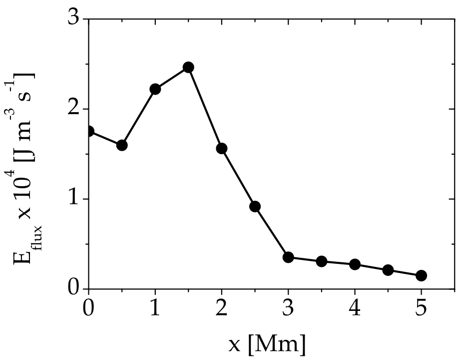

Fig. 12. Energy flux *vs.* horizontal direction for $A_v = 0.5$ km s^{-1} at $x = 0$ Mm.

Values of $E_{\rm flux}$ of the order of few thousands J m^{-3} s^{-1} that we obtain in our simulations are sufficient to heat a quiet corona. According to Withbroe and Noyes [30], to heat the solar corona, the vertical component of the energy flux should have $100 \sim 200$ J m^{-3} s^{-1}, while we get $E_{{\rm flux},x} = 3.3 \times 10^4$ J m^{-3} s^{-1} at $x = 3$ Mm (Fig. 11, left panel).

We found that the energy flux passing through the transition region is efficient to heat the lower corona. However the energy can be passed through the transition region by magnetoacoustic waves generated impulsively in the upper photosphere, they are not able to transport energy higher up.

4. Observations

We compare results of numerical simulations with analysis of observed plasma oscillations that took place in the symmetric and solitary sunspot of active group AR 11131 on December 8, 2010. This sunspot has been subject to intensive studies over a wide range of spectral wavelengths of the 3-min oscillation mode at 17 GHz (NoRH), using the correlation curves and synthesizing the two-dimensional radio and EUV, UV (SDO/AIA) images [1, 2, 31, 32]. Narrowband imaging of oscillation sources was made by applying the method of pixelized wavelet filtration (PWF) [33].

Based on the assumption of the vertical orientation of the magnetic field in the sunspot umbra and of the significant inclination of magnetic lines in the sunspot penumbra, we studied two types of spatial distribution of oscillation parameters (power, peak periods, and cut-off periods). The first assumption is related to the longitudinal distribution from the sunspot centre to its boundary; the second one, to height distribution. Height and longitudinal distributions of oscillations were obtained using 3D cube images from the observatory SDO/AIA at 304 Å, 171 Å and 1600 Å, 1700 Å. Narrowband imaging of oscillation sources was made in the rectangular coordinate system; we then adjusted it to the polar system. The coordinate system coincided with the centre of the sunspot umbra. A unit scanning angle was 1 deg, the duration of observation data set was 60 min, the value of periods varied from 120 s to 900 s (for the cadence time of 12 s), the image resolution in space was 0.6 arcsec.

Figure 13 presents calculated narrowband images of UV oscillation sources at 304 Å in the sunspot for three oscillation periods of 3, 5, and 14 min. Power of the main oscillation mode (3 min) is mostly in the sunspot umbra. No 3 min oscillations are observed beyond the umbra. As the period increases, power of oscillations gradually decreases starting from the centre. Near the period of 4–5 min, a ring-shaped source with a well-pronounced maximum oscillation power at the umbra/penumbra boundary is seen. Profile of the ring section for this range of periods is approximately a Gaussian shape with an abrupt decrease at the boundaries. As the oscillation period increases, the interior of the Gaussian keeps its inclination. The exterior starts flattening. The intensity peak is shifted and moves away from the centre. In Fig. 13, this shift is denoted by the enlarging vector as the distance between the moving dashed circle and the stationary boundary of the sunspot umbra increases. The shape of the shifting boundary follows the shape of the umbra boundary in details. It is noteworthy that our numerical findings also exhibit an increase of wave periods with the horizontal coordinate (Fig. 8).

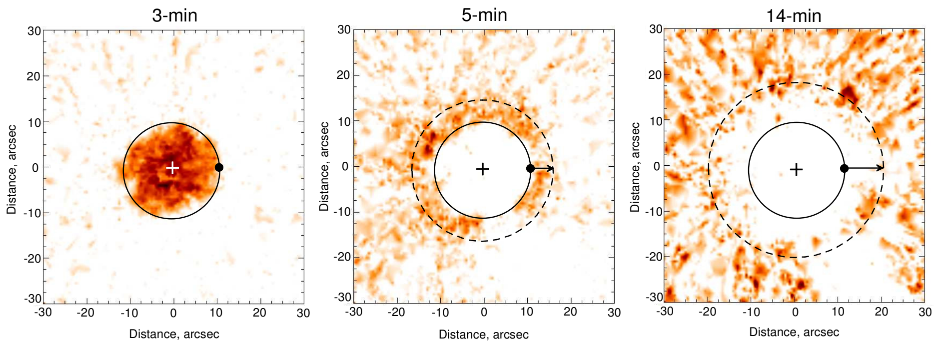

Fig. 13. The spatial structure of narrowband oscillation sources with periods of 3, 5, and 14 min above the sunspot of active group AR 11131 at 304 Å (SDO/AIA) on December 8, 2010. The solid circle shows the boundary of the sunspot umbra. The dashed circle shows the boundary of the external expanding zone of cut-off period. The increase of the approximate location of the umbra–penumbra boundary is denoted by the vector.

To obtain the continuous horizontal distribution of the oscillation power depending on the distance to the sunspot centre for different periods, the narrowband images were represented in the polar coordinate system and integrated over space in the range of periods from 120 to 900 s. Figure 14 presents the power distribution of the oscillation detected at 304 Å. The brightness of the contour plot depends on the oscillation power. The flat region of periods in the range from 120 to 135 s prevails up to the distance of 10 arcsec from the sunspot centre. The peak power (see Fig. 14, right panel) rapidly decreases with the distance away from the sunspot centre. In the umbra region, we see a less abrupt decrease ($\sim 12\%$) in oscillation power compared to the penumbra region ($\sim 26\%$). We have obtained the spatial distribution of cut-off wave periods as a boundary of the noise envelope (see Fig. 14, left panel) where the signal tends to zero. Ratio of cut-off period to peak period is flat in the vicinity of the umbra and diverge significantly in the penumbra region (see Fig. 14, right panel). This ratio varies within the range of 1.4 to 1.55, with the mean value of ~ 1.5 for the umbra region, and from 1.5 to 2.45, with the mean value of ~ 2 in the penumbra region.

Notice that values of cut-off wave periods presented in Fig. 14 for $\lambda =$ 304 Å similarly as in data obtained in our numerical simulations (Fig. 9, circles and diamonds) are in the range of 3–4 minutes in the umbra. We observe that wave periods obtained in numerical simulations (Fig. 9) essen-

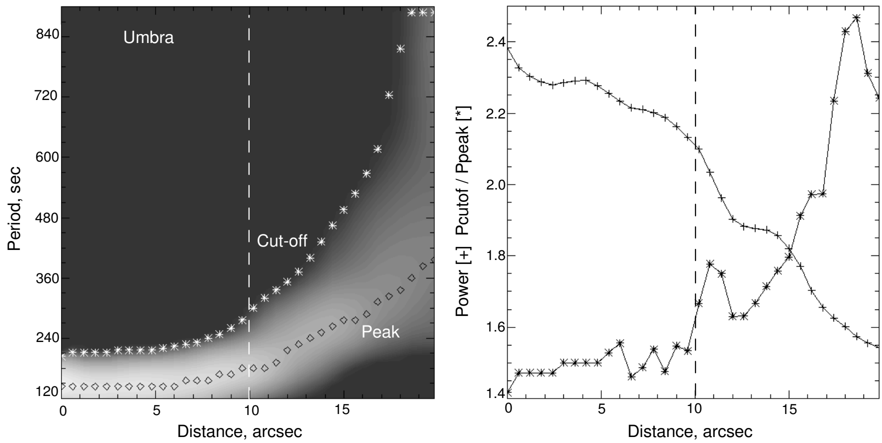

Fig. 14. Left panel: One-dimensional distribution of oscillation power for different periods at 304 Å (SDO/AIA), depending on the distance to the sunspot centre, on December 8, 2010. Stars mark the boundaries of the cut-off period; diamonds, the observed peak power. Right panel: Profiles of ratios of oscillation cut-off periods to their peak values [+] and peak power [*], depending on the distance to the sunspot centre. Periods are expressed in seconds; distance — in arcseconds. The vertical dashed line denotes the boundary of the sunspot umbra.

tially contain a range from $P = 160$ s to $P = 220$ s, while cut-off wave periods vary from $P = 200$ s up to $P = 220$ s in the same range of distance from the center of the sunspot.

To obtain the height distribution of wave periods in the region where the magnetic field is vertically directed (the sunspot umbra), we calculated the longitudinal distributions of oscillation power and the mean values for different wavelengths. The procedure was performed in the same way as that described above for 304 Å. We used 3D cube images obtained from SDO/AIA at different heights of generation of UV 1700 Å, 1600 Å, 304 Å, and EUV 171 Å bandpasses. According to the sunspot atmospheric model by Maltby *et al.* [34], emission of the EUV continuum at 1700 Å corresponds to the temperature minimum with temperature of about 5000 K and corresponding to the upper photosphere. Emission in the bandwidth of 1600 Å occupies the widest pass band, from the temperature minimum to the chromospheric C IV line, and corresponds to temperature of about 10^4 K. For the He II chromospheric line (304 Å), temperature increases with height with average formation temperature $T = 5 \times 10^4$ K. For the heights of the upper transition zone or lower corona, we observe the 171 Å (Fe IX) line with the plasma temperature of about 10^6 K.

Figure 15 shows the power distribution of peak oscillation periods calculated from the observed cut-off periods, according to Bel and Leroy [35], near the sunspot centre at 1700 Å, 1600 Å, 304 Å, and 171 Å. In the lower layers, at the photospheric level, the period value does not vary from the sunspot centre: its mean value is 163 s (2.72 min). The ratio between periods at the beginning and at the end of the distance is 1. As the height of emission generation becomes greater and the value of the peak period increases up to 169.8 s (2.83 min) at 1600 Å. At 304 Å, the value is 1.11 and value of the peak period is about 172.8 s (2.88 min). These values for the height of the corona at 171 Å are 177.0 s or 2.95 min, respectively. The results of numerical simulations also show increase of the wave periods with height (Fig. 8, crossed circles and diamonds). Values of P for large amplitude of the initial pulse ($A_v = 2$ km s^{-1}) coincide observational data obtained by Yuan *et al.* [1] (Fig. 8, full squares).

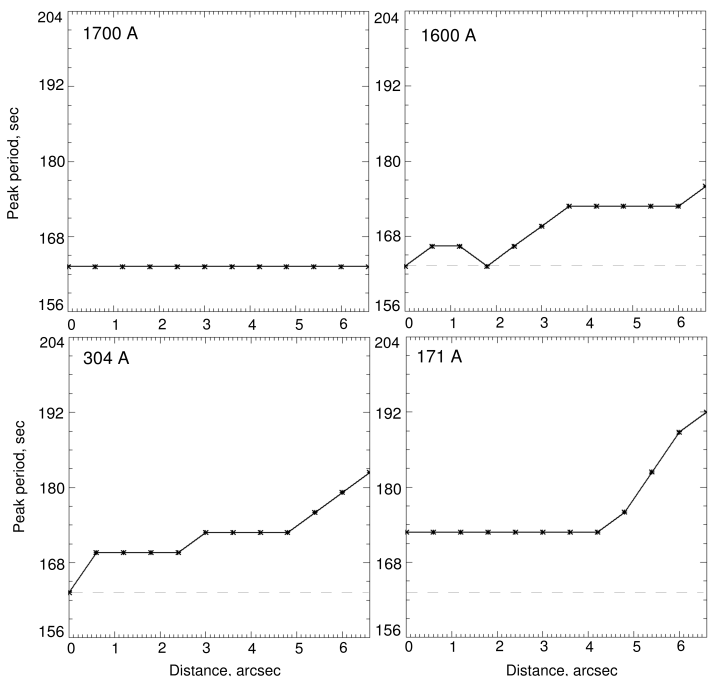

Fig. 15. Values of the calculated peak periods of emission oscillations for the vertical magnetic field, depending on the height of emission generation (SDO/AIA, 1700 Å, 1600 Å, 304 Å, and 171 Å) and on the distance to the centre of the sunspot umbra in AR 11131 on December 8, 2010. The horizontal dashed line shows the boundary of oscillation period at the temperature minimum level (1700 Å).

5. Conclusions

In this paper, we simulated numerically the behaviour of magneto-acoustic-gravity waves in the solar atmosphere that is permeated by a diverged with height magnetic field lines. These waves excited by the single initial pulse in vertical component of velocity equal to $V_y = 0.5$ km s^{-1} and $V_y = 2$ km s^{-1}, which corresponds to the granular motion, exhibit a periodicity that vary with height and horizontal distance. As they are ubiquitous in the region of sunspot, they are crucial in explanation of the plasma oscillation wave-period distribution. Moreover, slow magnetoacoustic-gravity waves, which follow the magnetic field lines, are able to transport hot plasma from the lower photosphere to the upper layers of the solar atmosphere and thereby can transport energy along field lines through the transition region to the solar corona. These reasons as well as their ubiquitous occurrence in the sunspots and active regions [36, 37], make them an additional channel of energy transport to the upper atmosphere layers beside Alfvén wave [38, 39] and magnetic reconnection [40].

We apply our numerical results to observations of the sole axisymmetric sunspot of active group AR 11131 on December 8, 2010. The 2D narrowband images of oscillation sources with periods of 3, 5, and 14 min show a dependence between the sources location, their form and the oscillation period. The observed dependencies can be explained by the spatial distribution of the magnetic field and its curvature in the framework of modification of the cut-off period [35]. We notice that the change in the inclination of magnetic lines results in the cut-off period increase [1, 41]. We observed waves with wave periods close to 3–4 min. For the penumbra region, we detected a sharp increase in wave periods, related to the increase in the longitudinal field component. This modification enables us to explain the penetration of the low-frequency component from the lower layers to the chromosphere and corona by the existence of inclined magnetic channels (wave-guides), along which slow magnetoacoustic waves propagate [42, 43].

Our findings for different heights of EUV emission generation at 1700 Å, 1600 Å, 304 Å, and 171 Å show that the ratio of calculated peak wave periods at the boundary of the sunspot umbra is larger than that at the centre. The ratio of these values for the temperature minimum (1700 Å) is 1.0; that for the transition zone (1600 Å) is about 1.07; for the chromosphere (304 Å), 1.11 and for the coronal level (171 Å), about 1.12. Values of the peak wave-period ratio are significantly lower than those observed in the penumbra region (~ 2.6). This implies a significant modification of peak wave periods with increasing inclination angles of the magnetic field in the penumbra and an insignificant modification for the vertical field component in the umbra. We observe that the mean value of wave periods grows with height: for 1700 Å (~ 163 s), for 1600 Å (~ 170 s), for 304 Å (~ 173 s), and for 171 Å ($\sim$ 177 s). In the distance-period profiles (Fig. 15), this is evident from the flattening and increasing of the peak periods in the sunspot umbra. Along with the increase in periods, an increase in oscillation power is observed. There is observed a minimum at 1700 Å (154.3) and 1600 Å (174.8), and maximum at the chromospheric level 304 Å (183.6), while at the level of the corona 171 Å (171.2), the value of the peak power decreases. These observational findings confirm the numerical simulations data where the peak periods and intensity of the waves propagating in the stratified atmosphere increase up to a certain height.

Obtained results show a partial agreement between the numerical findings for propagating pulses in the solar atmosphere with the diverged with height magnetic field and the observational data.

This work was supported by the Ministry of Education and Science of the Russian Federation. The authors are grateful to SDO teams for operating the instruments and performing the basic data reduction, and especially, for the open data policy. The work was partially supported by the Russian Foundation of Basic Research (RFBR), grants Nos. 13-02-00044, 13-02-90472, and 14-0291157. This research was supported by the Marie Curie International Research Staff Exchange Scheme Fellowship within the 7$^{\text{th}}$ European Community Framework Program. K.M.'s work was done in the framework of the project from the Polish National Foundation (NCN) grant No. 2014/15/B/ST9/00106. The software used in this work was in part developed by the DOE-supported ASCI/Alliance Center for Astrophysical Thermonuclear Flashes at the University of Chicago. The visualizations of the simulation variables have been carried out using the IDL (Interactive Data Language) software package.

REFERENCES

[1] D. Yuan, R. Sych, V.E. Reznikova, V.M. Nakariakov, *Astron. Astrophys.* **561**, A19 (2014).

[2] V.E. Reznikova, K. Shibasaki, R.A. Sych, V.M. Nakariakov, *Astrophys. J.* **746**, 119 (2012).

[3] P.M. Edwin, B. Roberts, *Sol. Phys.* **76**, 239 (1982).

[4] J.M. Fontenla, E.H. Avrett, R. Loeser, *Astrophys. J.* **406**, 319 (1993).

[5] S.M. Jefferies *et al.*, Low-frequency magneto-acoustic waves in the solar chromosphere, in: Proceedings of SOHO 18/GONG 2006/HELAS I, Beyond the Spherical Sun (ESA SP-624), 7–11 August 2006, Sheffield, UK, Eds. K. Fletcher, M. Thompson, p. 16.

[6] G.J.J. Botha, T.D. Arber, V.M. Nakariakov, Y.D. Zhugzhda, *Astrophys. J.* **728**, 84 (2011).

[7] P.S. Cally, T.J. Bogdan, *Astrophys. J.* **402**, 721 (1993).

[8] E. Khomenko, M. Collados, *Astrophys. J.* **653**, 739 (2006).

[9] T. Felipe, E. Khomenko, M. Collados, *Astrophys. J.* **719**, 357 (2010).

[10] E. Khomenko *et al.*, *Astrophys. J.* **694**, 411 (2009).

[11] R. Sych, V.M. Nakariakov, M. Karlicky, S. Anfinogentov, *Astron. Astrophys.* **505**, 791 (2009).

[12] R. Sych *et al.*, *Astron. Astrophys.* **577**, A43 (2015).

[13] P.F. Chen, E.R. Priest, *Sol. Phys.* **238**, 313 (2006).

[14] V.V. Zaitsev, A.V. Stepanov, *Sov. Astron. Lett.* **15**, 66 (1989).

[15] V.M. Nakariakov, C. Foullon, E. Verwichte, N.P. Young, *Astron. Astrophys.* **452**, 343 (2006).

[16] R. Centeno, M. Collados, J. Trujillo Bueno, *Astrophys. J.* **640**, 1153 (2006).

[17] R. Centeno, M. Collados, J. Trujillo Bueno, *Astrophys. J.* **692**, 1211 (2009).

[18] B.C. Low, *Astrophys. J.* **293**, 31 (1985).

[19] E.H. Avrett, R. Loeser, *Astrophys. J. Suppl.* **175**, 229 (2008).

[20] B. Fryxell *et al.*, *Astrophys. J. Suppl.* **131**, 273 (2000).

[21] D. Lee, A.E. Deane, *J. Comput. Phys.* **228**, 952 (2009).

[22] D. Lee, 2009, *Prog. Part. Nucl. Phys.* **63**, 117 (2009).

[23] D. Lee, *J. Comput. Phys.* **243**, 269 (2013).

[24] P. MacNeice, D.S. Spicer, S. Antiochos, A Model for Prominence Mass and Dynamics, in: Proceedings of 8$^{\text{th}}$ SOHO Workshop: Plasma Dynamics and Diagnostics in the Solar Transition Region and Corona, 22–25 June 1999, Paris, France, Eds. J.-C. Vial and B. Kaldeich-Schümann, p. 457.

[25] P. Konkol, K. Murawski, T.V. Zaqarashvili, *Astron. Astrophys.* **537**, A96 (2012).

[26] K. Murawski, A.K. Srivastava, T.V. Zaqarashvili, *Astron. Astrophys.* **535**, A58 (2011).

[27] Y. Suematsu, K. Shibata, T. Neshikawa, R. Kitai, *Sol. Phys.* **75**, 99 (1982).

[28] T.V. Zaqarashvili, K. Murawski, M.L. Khodachenko, D. Lee, *Astron. Astrophys.* **529**, A85 (2011).

[29] G. Vigeesh, V. Fedun, S.S. Hasan, R. Erdélyi, *Astrophys. J.* **755**, 18 (2012).

[30] G.L. Withbroe, R.W. Noyes, *Annu. Rev. Astron. Astrophys.* **15**, 363 (1977).

[31] R. Sych *et al.*, *Astron. Astrophys.* **539**, A23 (2012).

[32] R.A. Sych, V.M. Nakariakov, A.A. Anfinogentov, L. Ofman, *Sol. Phys.* **266**, 349 (2010).

[33] R.A. Sych, V.M., Nakariakov, *Sol. Phys.* **248**, 395 (2008).

[34] P. Maltby *et al.*, *Astrophys. J.* **306**, 284 (1986).

[35] N. Bel, B. Leroy, *Astron. Astrophys.* **55**, 239 (1977).

[36] T.J. Bogdan, P.G. Judge, *Phil. Trans. R. Soc. A* **364**, 313 (2006).

[37] B. Roberts, *Phil. Trans. R. Soc. A* **364**, 447 (2006).

[38] P. Chmielewski, K. Murawski, A.A. Solov'ev, *Res. Astron. Astrophys.* **14**, 855 (2014).

[39] P. Chmielewski, A.K. Srivastava, K. Murawski, Z.E. Musielak, *Acta Phys. Pol. A* **125**, 158 (2014).

[40] J. Birn, L. Fletcher, M. Hesse, T. Neukirch, *Astrophys. J.* **695**, 1151 (2009).

[41] I. De Moortel, A.W. Hood, *Astron. Astrophys.* **415**, 705 (2004).

[42] T.J. Wang, L. Ofman, J.M. Davila, J.T. Mariska, *Astron. Astrophys.* **503**, L25 (2009).

[43] M.S. Marsh, R.W. Walsh, S. Plunkett, *Astrophys. J.* **697**, 1674 (2009).

[44] J.E. Vernazza, E.H. Avrett, R. Loeser, *Astrophys. J. Suppl.* **45**, 635 (1981).